Dalton Transactions

ROYAL SOCIETY OF CHEMISTRY

PAPER

View Article Online
View Journal | View Issue

Cite this: *Dalton Trans.*, 2024, **53**, 17221

Effect of Co-doping on the electrochromic performance of hexagonal phase WO_3 nanorods†

Zhaozhu Qu,[a,b] Ankang Li,‡[b] Ming Gao,[d] Xiaohui Sun,[a,b] Xuyang Zhang, *[a,b] Guohua Wu*[a,b,c] and Xiangwei Wang*[a,b]

Received 15th August 2024,
Accepted 30th September 2024

DOI: 10.1039/d4dt02319f

rsc.li/dalton

In this study, cobalt-doped hexagonal phase WO_3 nanorods were prepared by a template-free hydrothermal method. The effects of varying the cobalt doping concentration on the microscopic morphology and electrochromic properties of hexagonal phase WO_3 films were investigated. Films synthesized with the optimal cobalt element doping concentration demonstrate a notable improvement in their electrochromic properties compared to the pure hexagonal phase WO_3 films. The film doped with 1.5% Co exhibited excellent cycling stability, retaining 98.55% of its original value after 500 cycles. The introduction of cobalt results in the formation of a nanorod structure with a high specific surface area within the film. This structure provides additional reaction sites for the electrochromic reaction process, thereby enhancing the optical modulation and coloration efficiency of WO_3. The resulting films with excellent electrochromic properties provide a convenient and effective means for ion-doped modification of WO_3-based electrochromic films.

1 Introduction

In the context of the ongoing modernization of urban environments, energy consumption in building operations has emerged as a significant social and environmental challenge.[1] The deployment of energy-saving smart glass and the promotion of green energy-saving technologies represent pivotal initiatives in reducing heat loss from windows and doors, thereby lowering overall energy consumption in buildings.[2,3] Energy-saving smart glass refers to materials that undergo stable and reversible changes in their optical properties upon the application of an external electric field or current. This is evidenced by a reversible alteration in the transmittance of the material in the visible and near-infrared wavelengths,[4] thereby enabling subjective dynamic control of visible light. It is currently the most promising energy-saving smart window technology for large-scale commercial production. As a representative inorganic electrochromic material, WO_3 has become a hotspot in the field due to its exceptional electrochromic properties and diverse range of applications in related technical fields.[5–7] However, the lower optical modulation amplitude and unsatisfactory cycling stability remain significant limitations for WO_3 materials in advancing towards mature applications.[8,9] Therefore, to address the pressing issue of energy consumption and to accommodate the evolving application scenarios, the development of WO_3-based electrochromic materials with superior and comprehensive properties has become a primary objective of contemporary research.

The optimization of WO_3-based electrochromic materials involves the enhancement of ion and electron insertion and extraction processes, with a particular emphasis on the optimization of ion insertion and extraction mechanisms. The enhancement of the electrochromic performance of WO_3 relies on improving ion conductivity and reducing ion trapping. This may be accomplished through the manipulation of micromorphology, the adjustment of crystallinity, the introduction of ion doping, and the design of composite structures.[10,11] Individual modification techniques typically target specific properties, while a combination of methods is expected to yield WO_3 electrochromic materials with superior overall properties.

The physical phase structure of a crystal is a critical determinant of the properties exhibited by a given material. The crystal structure of WO_3 can be classified as one of four types: cubic, monoclinic, orthorhombic, or hexagonal. These classifications are based on the different connections of the WO_6 octahedra.[12] The diverse crystal structures exert a direct influ-

[a]*College of Materials Science and Chemical Engineering, Harbin Engineering University, Harbin, 150001 Heilongjiang, China. E-mail: xuyangz@hrbeu.edu.cn, ghwu@hrbeu.edu.cn, wangxiangwei@hrbeu.edu.cn*
[b]*Qingdao Innovation and Development Base of Harbin Engineering University, Harbin Engineering University, Qingdao 266500, Shandong, China*
[c]*The Key Laboratory of Functional Molecular Solids, Ministry of Education, PR China*
[d]*Ludwig-Maximilians-Universität München, Geschwister-Scholl-Platz 1, 80539 Munich, Germany*

†Electronic supplementary information (ESI) available. See DOI: https://doi.org/10.1039/d4dt02319f

‡Co-first author.

ence on the process of ion insertion and extraction. In recent years, there has been a notable increase in the number of studies focusing on the modulation of the crystal structure of WO_3.[13,14] The objective of these studies has been to enhance the electrochromic properties of WO_3 by introducing a hexagonal phase structure into the interior of the material.[12,15,16] The hexagonal phase structure of WO_3 comprises numerous triangular, tetragonal, and hexagonal channels, which facilitate enhanced ion transport rates and provide additional reaction space for electrochemical reactions.[17,18] Furthermore, the small size and interstitial gaps of the material enable it to withstand the stress and strain caused by the reaction process, thereby avoiding the volume expansion that typically occurs during electrochromic reactions. This ensures good cycling stability and a higher reversible capacity for electrochromic materials.[19] Therefore, the incorporation of a hexagonal phase structure within WO_3 represents a promising avenue for improving its electrochromic properties. It is noteworthy that numerous studies indicate that the morphology of the majority of hexagonal WO_3 exhibits a one-dimensional (1D) structure, particularly in samples synthesized *via* the hydrothermal method.[16,20] Compared to WO_3 particles that have been synthesized using the conventional hydrothermal method, 1D nanostructures have been observed to possess advantages such as higher specific surface areas, superior mechanical properties, enhanced substrate adhesion, and increased ionic conductivity.[21,22] Furthermore, these nanostructures generate a substantial number of polarons and exhibit the localized surface plasmon resonance (LSPR) effect, thereby enhancing ion diffusion and absorption of visible and near-infrared light, which is a highly desirable property in the field of electrochromism.[23] Nevertheless, the prefabrication of hexagonal WO_3 is hindered by inherent complexities, and its electrochromic properties require further optimization.

In addition, ion doping of WO_3 represents an effective method for enhancing its electrochromic properties, whereby the internal crystal structure is modulated.[24,25] Cobalt, with an ionic radius similar to that of tungsten, can improve the ion channels within the crystal structure without causing significant lattice distortions.[26] Furthermore, the introduction of cobalt ions can create additional defective states within the film, providing active sites for ionic redox reactions and enhancing its cycling stability while also improving the optical modulation amplitude.[27,28] This approach is anticipated to result in a mutual enhancement of the electrochromic performance.

The simultaneous enhancement of the performance of WO_3 electrochromic materials in terms of cycling stability, optical modulation, and coloring efficiency poses a significant challenge. This study proposes a novel approach for the preparation of doped hexagonal WO_3 nanorod thin films through a one-step hydrothermal synthesis. The introduction of the hexagonal phase crystal ensures excellent cycling stability, whereas the integration of a nanorod structure and Co doping facilitates enhanced optical modulation and coloring efficiency in WO_3 electrochromic materials. The simplified single-step hydrothermal process offers a streamlined approach for composite modification, eliminating the complex steps required for introducing hexagonal crystals *via* seed layers. Hexagonal WO_3 nanorods with varying Co doping ratios have been successfully prepared. Among these, the 1.5% cobalt-doped WO_3 film exhibits high transmittance modulation, fast response time, large coloring efficiency, and good cycling stability, making it an ideal candidate for energy-saving smart glass.

2 Experimental section

2.1 Chemical reagents and materials

Tungsten acid (H_2WO_4), hydrogen peroxide (H_2O_2), hydrochloric acid (HCl), cobalt nitrate hexahydrate ($Co(NO_3)_2{\cdot}6H_2O$), lithium perchlorate ($LiClO_4$), propylene carbonate (PC), acetone, and anhydrous ethanol were purchased from commercial sources and used without any further purification. Fluorine-doped tin oxide (SnO_2) glass substrates (25 × 50 × 2.2 mm) were chosen and cleaned using ultrasonication in acetone, ethanol and anhydrous ethanol for 30 min, followed by drying in an oven at 60 °C. The electrolyte used in this study was 0.25 M $LiClO_4$/PC solution.

2.2 Preparation of precursor solution

The synthesis of hexagonal WO_3 using solvothermal methods has been previously reported.[29] The specific preparation of the precursor fluids used in this study is as follows: A solution of 2.5 g of H_2WO_4 was prepared by dissolving the compound in a mixture of 60 mL of deionized water and 20 mL of 30 wt% hydrogen peroxide. The solution was then heated in a water bath at 95 °C with continuous stirring. Once the solution had become clear, deionized water was added to dilute the clarified solution to a final volume of 200 mL, resulting in a precursor solution of peroxotungstic acid (PTA) with a concentration of 0.05 M.

2.3 Preparation of Co-doped WO_3 films

A solution comprising 6 mL of PTA, 1 mL of HCl (6 M), and 6 mL of acetonitrile was added to 24 mL of deionized water. Then, different molar ratios of cobalt sources (0%, 0.5%, 1.0%, 1.5%, 2.0%) were introduced into the precursor solution and stirred for 30 minutes at room temperature. This mixture was then transferred into a 100 mL polytetrafluoroethylene hydrothermal autoclave liner. A cleaned FTO glass was placed in the liner at a specific angle, with the conductive side oriented in a downward direction. The autoclave was then heated to 180 °C and maintained at that temperature for 12 hours. After the reaction was completed, the FTO glass was removed, rinsed with deionized water, and dried in an oven at 60 °C. Based on the amount of cobalt source used, the prepared films were labeled as WCo-0%, WCo-0.5%, WCo-1.0%, WCo-1.5%, and WCo-2.0%. The schematic diagram of the formation process is shown in Fig. 1.

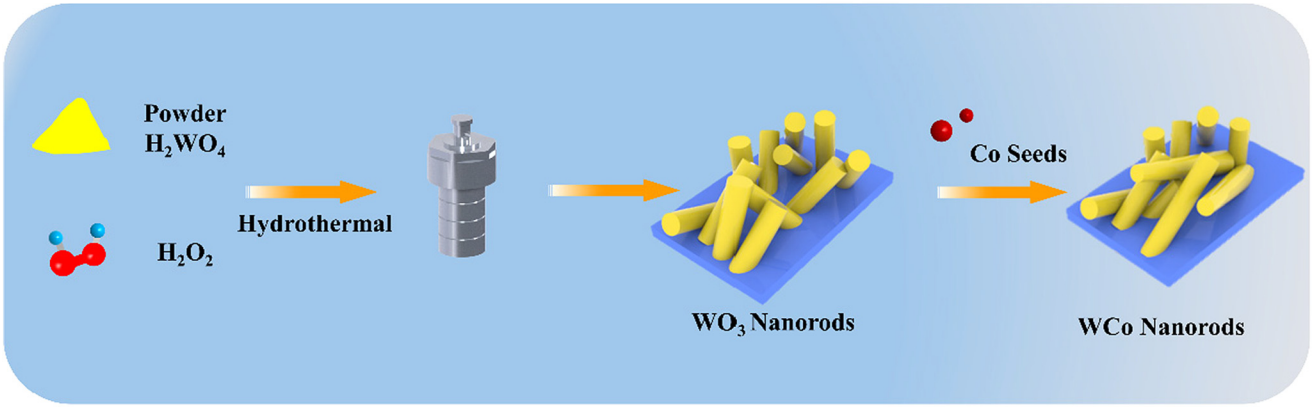

Fig. 1 Schematic diagram of the formation process of Co-doped WO_3 nanorods prepared by a hydrothermal method.

2.4 Characterization

The X-ray diffraction (XRD) analysis of the composites was conducted using a Rigaku MiniFlex600 to determine their phases and crystal structure. The XRD analysis was performed using Cu Kα radiation with a scanning angle range of 10–80° and a scanning speed of 5° min^{-1}. The growth morphology and microstructure of the films were characterized by scanning electron microscopy (SEM, Zeiss Sigma 300) and transmission electron microscopy (TEM, FEI Tecnai G2 F20). X-ray photoelectron spectroscopy (XPS, Thermo Scientific K-Alpha) was employed to analyze the elemental composition and valence states in the films. Al Kα X-ray was used as the excitation source in XPS instruments with $h\nu$ = 1486.6 eV. The pass energies used for the full-spectrum scan and high-resolution scans were 150.0 eV and 50.0 eV, with energy step sizes of 1.0 eV and 0.1 eV, respectively. When fitting the high-resolution XPS data using the Thermo Advantage software, the binding energy of C1s = 284.80 eV was used as the energy reference for charge correction. The optical properties in the wavelength range from 380 nm to 1100 nm and the response kinetics at a wavelength of 633 nm were investigated by coupling a fiber optic spectrometer (AvaSpec-vaLight-DH-S-BAL) and an electrochemical workstation (CHI660E), with applied voltages of −1.5 V and 0.5 V, respectively. The electrochemical properties of the films were tested using a three-electrode system, comprising a Pt sheet as the counter electrode, an Ag/AgCl electrode as the reference electrode, an FTO glass with the electrochromic film as the working electrode, and 0.25 M $LiClO_4$/PC solution as the electrolyte.

3 Results and discussion

In order to investigate the crystallinity and physical structure of the thin films, the prepared WO_3 films were characterized by X-ray diffraction (XRD). The XRD patterns of WO_3 thin films with different cobalt doping contents are shown in Fig. 2. The WO_3 films synthesized directly *via* hydrothermal methods on FTO glass substrates match well with h-WO_3 (JCPDS 33-1387).

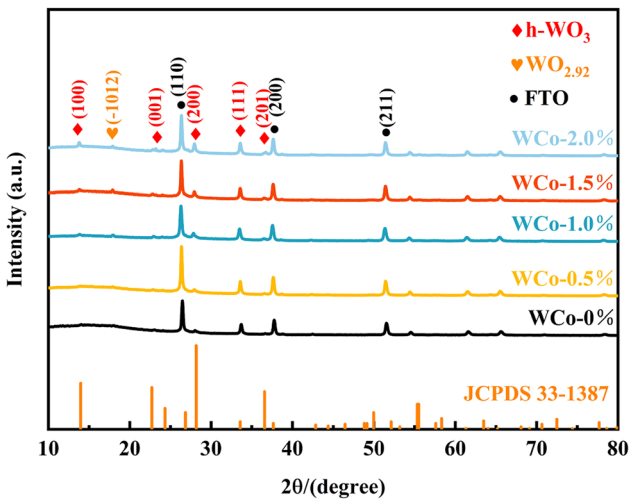

Fig. 2 XRD patterns of Co-doped WO_3 films with different Co contents.

The characteristic diffraction peaks at 13.957°, 22.718°, 28.172°, 33.575°, and 36.572° correspond to the (100), (001), (200), (111), and (201) crystal planes of the hexagonal phase structure, respectively. It is noteworthy that the crystal structure of the films remains unaltered with increasing cobalt doping ratios. Instead, the intensities of the diffraction peaks were consequently enhanced, indicating a tendency for preferential growth on the (200) crystal plane.[30] This suggests that the crystallinity of the films increased following cobalt ion doping.[31] In addition, the introduction of cobalt ions resulted in the emergence of the (−1012) crystalline surfaces in the XRD pattern, which corresponded to monoclinic polycrystalline $WO_{2.92}$ (JCPDS 30-1387). Furthermore, the (100) and (200) crystal planes of the films also shifted to lower values with increasing cobalt ion contents. The emergence of $WO_{2.92}$ and the alteration in the crystal plane spacing provide compelling evidence for the successful introduction of cobalt ions into the WO_3 lattice.[32]

Fig. 3 shows the SEM images of WCo-0% and WCo-1.5% nanorods at different magnifications. As shown in Fig. 3a and

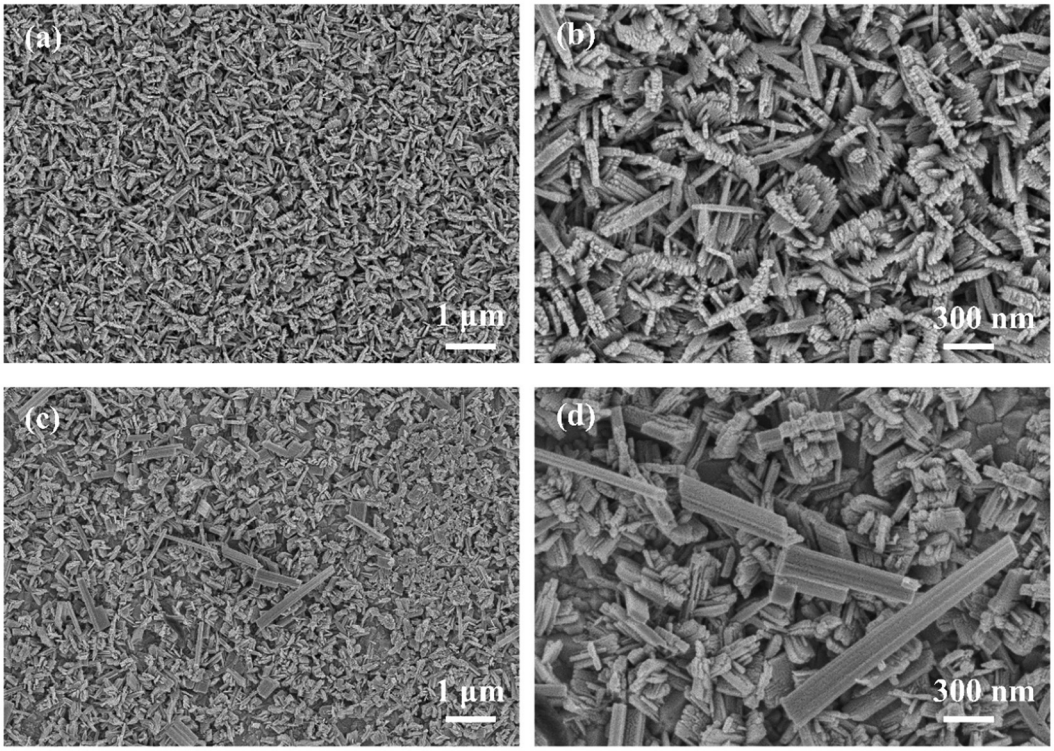

Fig. 3 SEM images of (a and b) WCo-0%, (c and d) WCo-1.5% with different magnifications.

b, the WCo-0% nanorods exhibit a diameter of approximately 30 nm and a length range of 100–300 nm. Fig. 3c and d illustrate the morphology of WO_3 nanorods with 1.5% cobalt doping (WCo-1.5%). Compared with pure WO_3, the cobalt-doped WO_3 nanorods display a more irregular surface and larger crystal sizes, with a diameter of approximately 100 nm and lengths of 600–1000 nm. A comparison of the WO_3 films with different cobalt doping ratios (Fig. S1†) reveals that the surface of the WO_3 nanorods exhibits minimal alteration at a doping content of 0.5% cobalt ions. Upon increasing the doping content of cobalt ions to 1.0%, the formation of large-sized nanorod structures within the film became evident. Upon further increasing the cobalt ion doping content to 2.0%, the nanorods began to grow in a parallel arrangement, forming a plate-like structure. Additionally, the average length of the nanorods reached the micrometer scale. Furthermore, the nanorod structure of the WO_3 films was well maintained across different cobalt ion doping ratios.

The change in the crystal morphology is attributed to the introduction of cobalt ions, which modifies the growth orientation of a part of the nanorod structure. Consequently, a denser arrangement of the nanorods and an increase in the diameter of the nanorods in the transverse alignment direction are observed.[28] At the same time, some of the WO_3 nanorods undergo optimal growth along the longitudinal direction, resulting in an increase in the nanorod sizes. It is noteworthy that the rough nanorod morphology facilitates an increased contact area between the electrochromic material and the ions, thereby allowing a large number of ions and electrons to complete the embedding and detachment process. The closely aligned nanorod structure also enhances the structural stability of the films, which plays an important role in improving the cycling stability of the WO_3 films.[29,33]

The formation mechanism of the WO_3 nanorods can be explained by the following chemical reaction equation:[34]

$$H_2WO_4 + xH_2O_2 \rightarrow WO_3 \cdot xH_2O_2 \cdot xH_2O \text{ (peroxotungstic acid)} \quad (1)$$

$$WO_3 \cdot xH_2O_2 \cdot xH_2O \rightarrow WO_3(\text{nucleus}) + (x+1)xH_2O + (1/2)xO_2 \uparrow \quad (2)$$

In the precursor solution, H_2O_2 reacts with H_2WO_4 to form peroxotungstic acid (PTA). At 180 °C, the hydrothermal conditions exceed the critical decomposition temperature of PTA,[34] resulting in the formation of WO_3 nuclei on the surface of the FTO substrate. These nuclei serve as growth sites for the subsequent formation of rod-like structures.[33] The smaller lattices, with their large specific surface areas, gradually accumulate on the surface of the FTO substrate, eventually forming nanorod-like structures.[35]

The microscopic morphology of the WCo-0% and WCo-1.5% films was investigated in detail using transmission electron microscopy. As shown in Fig. 4a, the nanorods of the WCo-0% films have a diameter of approximately 30 nm and exhibit complete crystallinity along their entire length, characterized by distinct lattice fringes. The corresponding high-resolution transmission electron microscopy (HRTEM) image in Fig. 4b reveals that the WO_3 nanorods have a lattice spacing

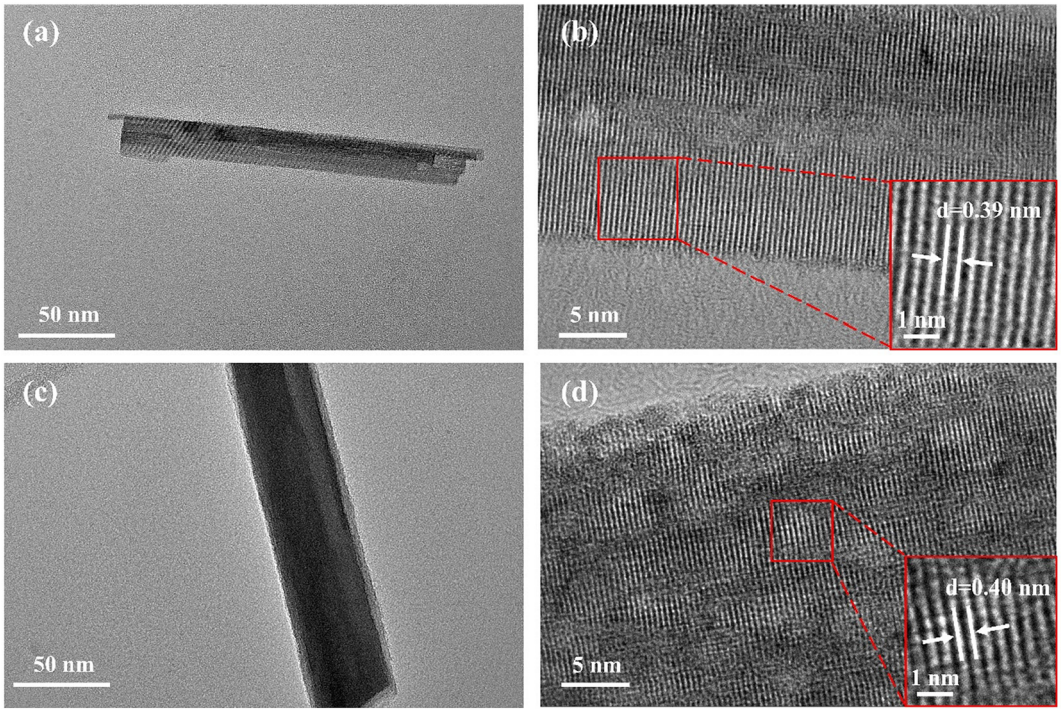

Fig. 4 TEM images of (a) WCo-0% and (c) WCo-1.5% and (b and d) the corresponding HRTEM images.

of 0.39 nm, which correlates to the (200) crystallographic plane of the hexagonal-phase WO_3. This suggests that the nanorods grow preferentially along the (200) crystallographic direction, which is consistent with the conclusions obtained from XRD analysis.

Fig. 4c shows the morphology of WO_3 nanorods doped with 1.5% cobalt ions, demonstrating a notable increase in surface roughness following the introduction of cobalt ions. This observed roughness can be attributed to the presence of defects and irregularities at the nanoscale, which are caused by differences in the ionic radii between the ions.[36] The additional lattice defects and vacancies created by doping facilitate further full contact with the electrolyte and provide additional sites for ion insertion and removal.[37] Additionally, the lattice spacing of 0.40 nm, as observed in Fig. 4d, corresponds to the (200) crystal plane of hexagonal WO_3. The observed increase in lattice spacing in the WCo-1.5% films can be attributed to the introduction of cobalt ions, whereby Co^{2+} ions are incorporated into the WO_3 lattice, replacing W^{6+} ions. Fig. 5 shows the EDX spectrum of WCo-1.5%, confirming the presence of Co and its uniform distribution throughout the Co-doped WO_3 nanorods.

X-ray photoelectron spectroscopy (XPS) measurements were conducted to investigate the chemical composition of the films at different cobalt ion doping concentrations. Fig. 6a examines the chemical valence state of elemental W within the film at various cobalt ion doping levels, showing that the spectral peak of W4f shifts towards higher binding energies with increasing cobalt ion doping contents. This shift is primarily due to a change in the Fermi energy level resulting from the alterations in the concentration of oxygen vacancies. It is well known that the presence of oxygen vacancies in the WO_3 crystal structure introduces states between the forbidden gap and the conduction band, resulting in a shift of the Fermi energy level towards higher energies.[38] The peaks at 35.5 eV, 37.6 eV, and 41.4 eV in the high-resolution XPS spectra of W4f correspond to the $W^{6+}4f_{7/2}$, $W^{6+}4f_{5/2}$, and $W^{6+}5p_{3/2}$ spin–orbit double peaks, respectively.[31,39] The peaks appearing at 34.28 eV and 35.92 eV are attributed to the $W^{5+}4f_{7/2}$ and $W^{5+}4f_{5/2}$ orbitals, respectively. The presence of the W^{5+} peaks indicates that the cobalt-ion doped films are sub-stoichiometric, suggesting that the introduction of cobalt ions has resulted in a modification of the valence state of the W element within the films.[26] Furthermore, the ratio of W^{5+}/W^{6+} is indicative of the concentration of oxygen vacancies within the film.[31] By fitting the peak area ratios of W^{5+} and W^{6+}, it was found that with the introduction of cobalt ions, the ratio of W^{5+}/W^{6+} increased from the original 0.12 to 0.14, further demonstrating that the concentration of oxygen vacancies within the film increases with cobalt ion doping. As shown in Fig. 6b, the XPS energy spectrum of the film with 1.5% cobalt ion doping concentration contains signals only from elements C, W, O, and Co, with no other elements detected. Fig. 6c shows the Co2p elemental spectrum within the WCo-1.5% film, with peaks at 778.4 and 793.7 eV, which correspond to $Co^{2+}2p_{3/2}$ and $Co^{2+}2p_{1/2}$, respectively.

The cyclic voltammetry (CV) curves of the WO_3 films in 0.25 M $LiClO_4$/PC electrolyte with different cobalt doping ratios were obtained to investigate the electrochemical behavior. As shown in Fig. 7a and b, the CV curves of the sample films at

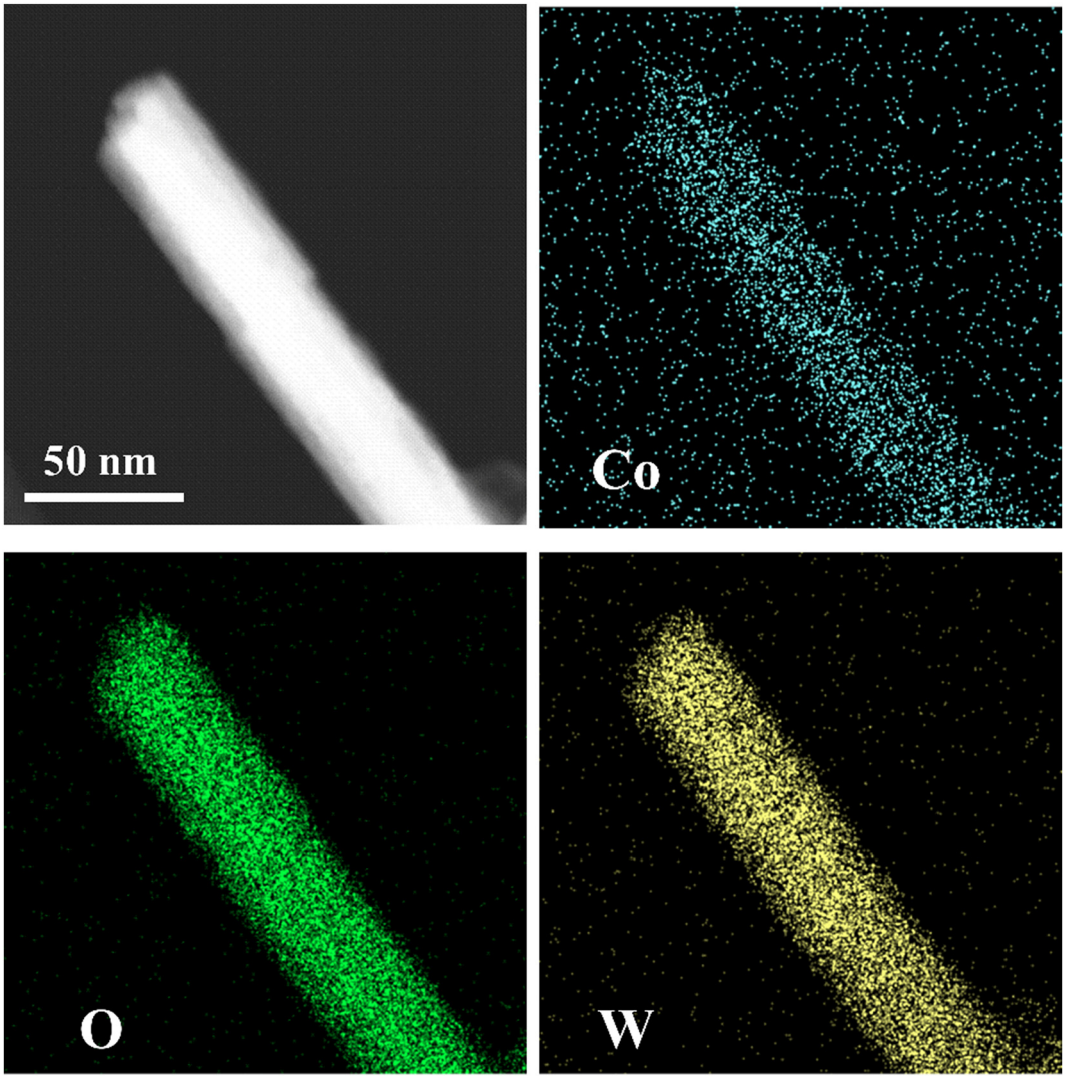

Fig. 5 EDX spectrum of WCo-1.5%.

all ratios exhibit a high degree of similarity. The WO_3 films with various cobalt doping ratios display distinct anodic and cathodic peaks. The anodic peak around −0.5 V corresponds to the oxidation of the low valence W^{5+} to W^{6+}, resulting in the film exhibiting a bleached state. Conversely, the cathodic peak appearing between −0.75 V and −1.0 V corresponds to the coloring process of the WO_3 film. This indicates the reduction of W^{6+} to W^{5+} during cathodic polarization, which is driven by the insertion of Li^+ into the film. The specific ion insertion and extraction processes are described by the following reaction equations:

$$WO_3\ (\text{bleached}) + xLi^+ + xe^- \rightleftharpoons Li_xWO_3\ (\text{colored}) \quad (3)$$

As shown in Fig. 7c, the area enclosed by the CV curves of all samples is significantly larger compared to WCo-0%. Additionally, the position of the anodic peak current exhibits a slight positive shift upon the introduction of cobalt ions into the film. The incorporation of cobalt ions has a marked effect on the oxygen vacancy concentration and the microscopic morphology of the films. The resulting nanostructures, with their high specific surface areas, provide additional reaction sites for the insertion and extraction of lithium ions during the electrochromic process. Furthermore, Fig. 7c demonstrates that the anodic and cathodic current densities of the WO_3 films reached an optimized maximum with a cobalt ion concentration of 1.5%. However, excessive doping with cobalt ions led to a noticeable decrease in the current density of the film (Fig. S2†). This indicates that an excess amount of cobalt forms a layer of cobalt tungsten oxide on the film surface, which impedes the migration of Li^+ ions during the electrochromic reaction.[32]

Moreover, the relationship between the peak current density and the square root of the scan rate ($v^{1/2}$), as illustrated in Fig. 7d, demonstrates a strong linear correlation, indicating that the overall reaction is a process controlled by diffusion.[39] Additionally, WCo-1.5% exhibits a larger slope compared to

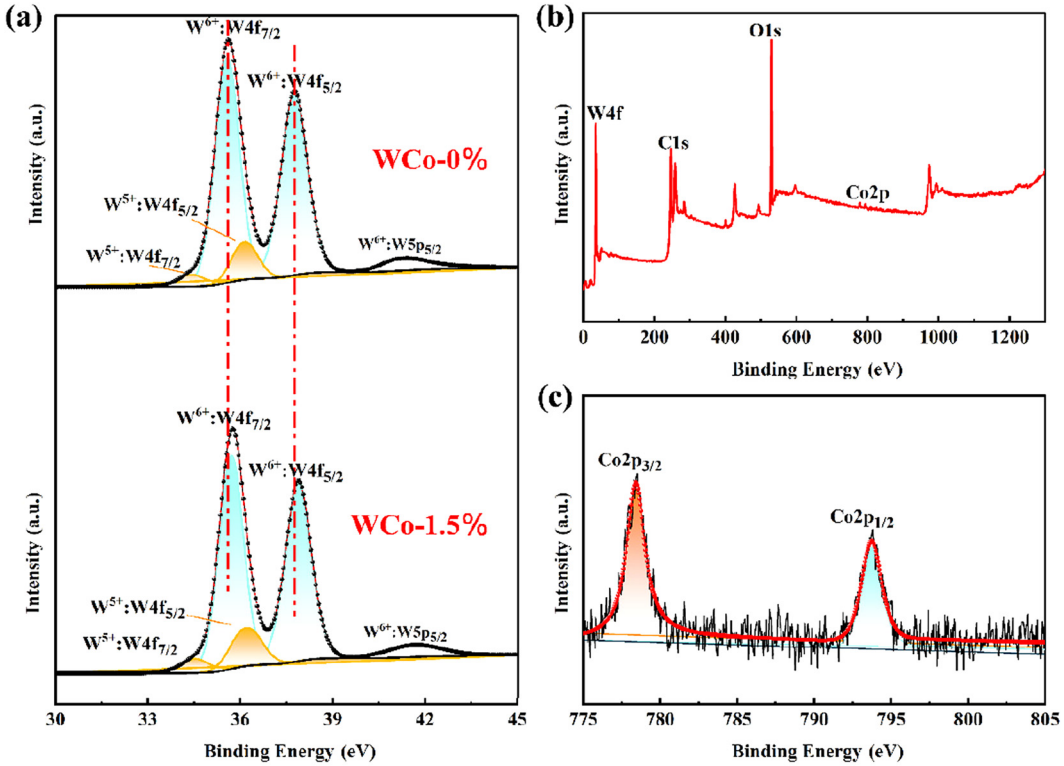

Fig. 6 (a) W4f spectra of WO_3 and WCo-1.5% films, (b) total survey and (c) Co2p spectrum of the WCo-1.5% film.

WCo-0%, suggesting an increased diffusion coefficient for Li^+ ions and a shorter diffusion pathway within the film.[40]

Generally, optical modulation is a principal metric for assessing the electrochromic performance of WO_3 films. To evaluate the effect of cobalt ion introduction on the optical properties of the samples across visible and near-infrared wavelengths, the transmittance spectra of the film samples were recorded over a wavelength range of 380 nm to 1100 nm. This was conducted using a three-electrode system with −1.5 V (colored state) and +0.5 V (bleached state) voltages applied for 60 seconds, respectively, as shown in Fig. 8a and b. Fig. 8a indicates that the optical modulation ($\Delta T = T_b - T_c$, where T_b and T_c represent the optical transmittance of the film in the bleached and colored states, respectively) of the WCo-0% film at the wavelength of 633 nm is only 30.73% (T_b = 83.53%, T_c = 52.80%). Meanwhile, the optical modulation of the WCo-0% films at 890 nm within the NIR range is 39.24%. For the WCo-1.5% sample, the initial overall transmittance at 633 nm in the bleached (T_b) state is 71.49%, which is lower than that for WCo-0%. This decrease can be attributed to increased light scattering in the films, which is a consequence of enhanced crystallinity resulting from cobalt doping and the formation of cobalt oxides on the film surface.[41] The optical transmittance at the same wavelength for the colored (T_c) state is 5.22%. Consequently, the maximum optical modulation achieved is 66.27% at 633 nm (Fig. 8b), with the optimal modulation amplitude reaching 72.57% at 890 nm. The illustrations in Fig. 8b are optical photographs corresponding to the colored state and bleached states of WCo-1.5%, respectively. This performance is superior to that of the WCo-0% film. However, an increase in the doping concentration of cobalt ions to 2.0% resulted in a 44.49% reduction in the optical modulation of the film within the visible wavelength range (Fig. S3†). This decline can be attributed to two key factors. Firstly, the modification of some cobalt ions within the lattice results in the formation of excess residual cobalt species, which adhere to the surface of the film and form cobalt oxides. This accumulation hinders the transport of Li^+ ions during the electrochromic reaction. Secondly, the excessive insertion of cobalt ions into the WO_3 lattice results in significant lattice distortion, which leads to a notable degradation of the optical properties of the WO_3 films. Detailed optical modulation data for WO_3 films at 633 nm and 890 nm with various cobalt ion doping concentrations are provided in Table 1.

Switching time is defined as the time required for the change in optical transmittance of the WO_3 film to reach 90%. Fig. 8c and d illustrate the *in situ* transmittance variation at 633 nm for both films, measured at voltages of −1.5 V and +0.5 V. As seen in Fig. 8c, the response time of the WCo-0% film is shorter than that of the doped film, with the coloring time (t_b) and bleaching time (t_c) measured at 12.28 s and 4.82 s, respectively. Notably, the introduction of cobalt ions into the film results in an increase in the switching time, with coloring and bleaching times of 20.78 s and 6.73 s, respectively, as shown in Fig. 8d. The continued introduction of cobalt ions leads to even more unfavorable switching times (Fig. S4†). This

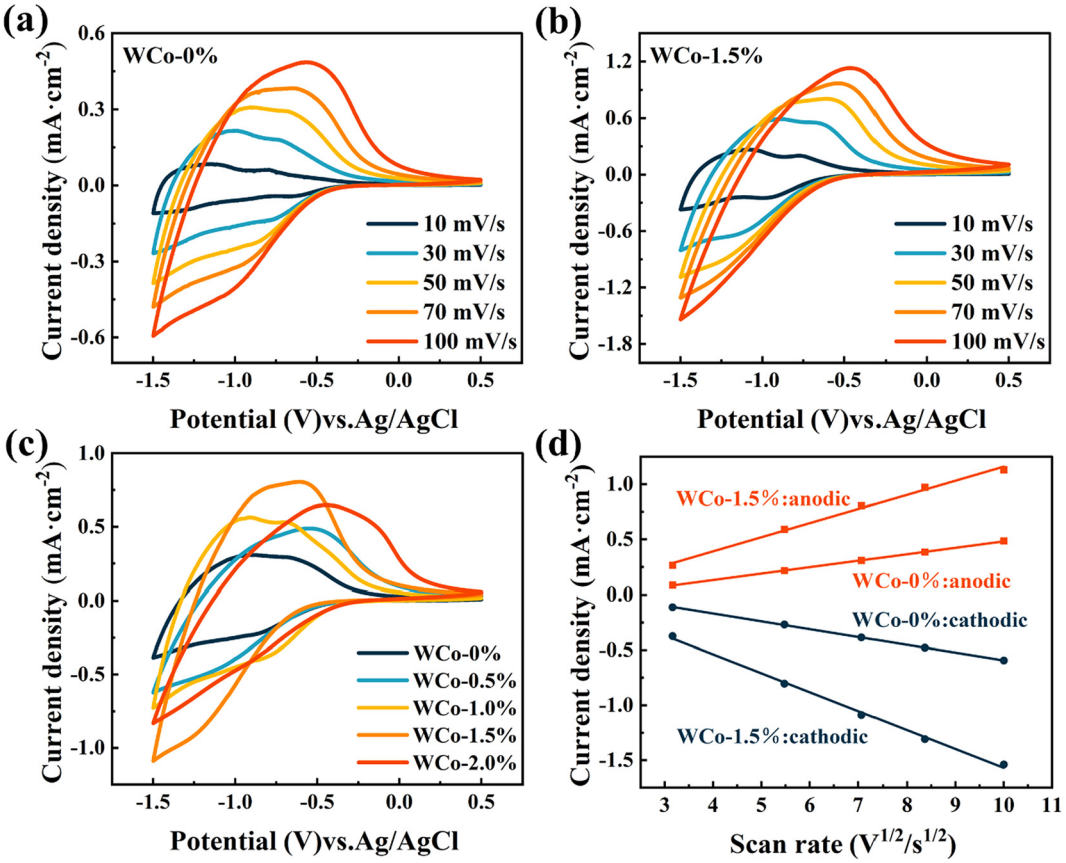

Fig. 7 Cyclic voltammetry (CV) curves of (a) WO_3 and (b) WCo-1.5% films at different scan rates between −1.5 V and +0.5 V; (c) cyclic voltammetry (CV) curves of WO_3 films at different cobalt doping ratios (50 mV s^{-1}); (d) peak current density *versus* square root of the scan rate.

degradation can be attributed to the increase in the specific surface area, which enhances the contact area between the film and the electrolyte, thereby increasing the demand for active sites and ions to participate in the electrochromic reaction. Additionally, the excessive introduction of lithium ions is hindered by the formation of cobalt oxides on the surface of the film, which plays a significant role in the degradation of its switching time.

The coloration efficiency (CE) stands as another crucial metric for evaluating the electrochromic performance of WO_3 films. It is defined as the ratio of the change in the optical density (ΔOD) to the change in unit charge density (ΔQ) inserted within a designated film area at a particular wavelength. This metric can be determined by employing the following formula:

$$CE = \Delta OD/\Delta Q = \log(T_b/T_c)/Q/S \quad (4)$$

where T_b and T_c represent the optical transmittance of the film in its bleached and colored states, respectively, Q is the charge density during the coloring process, and S is the electrode area. A comparison of the coloration efficiencies is illustrated in Fig. 8e and f. Following the introduction of cobalt ions, the CE values of WO_3 films increased significantly from 43.10 cm^2 C^{-1} to 80.36 cm^2 C^{-1}. The enhanced CE values indicate that the films can achieve a substantially improved range of optical transmittance with lower charge insertion or extraction.

Finally, to assess the cycling stability of WO_3 films with varying ratios of cobalt ion doping, a CV test was conducted for 500 cycles in a 0.25 M $LiClO_4$/PC electrolyte solution. The CV curves and transmittance spectra in the visible and NIR wavelengths, both before and after the CV cycling test, are presented in Fig. 9. As illustrated in Fig. 9a, the WCo-0% film exhibits remarkable cycling stability, retaining 93.18% of its original CV curve even after 500 cycles. This stability can be attributed to the film's inherent hexagonal phase structure, which provides superior structural integrity. In addition, the optical modulation depicted in Fig. 9c experienced a slight decline, from an initial 30.73% to 30.67%. Nevertheless, it retained 99.80% of its original state. In contrast, the introduction of cobalt ion doping in the WO_3 film resulted in a reduction of optical modulation from 66.27% to 65.31% after 500 CV cycles, achieving a retention rate of 98.55% (Fig. 9b and d). It is encouraging that the cycling stability of cobalt doped WO_3 films in the NIR wavelength range is also significantly enhanced compared to the WCo-0% film. However, the addition of excessive amounts of cobalt ions to the WO_3 lattice results in severe distortions, which in turn leads to a drastic decrease in cycling stability, as shown in Fig. S6.†

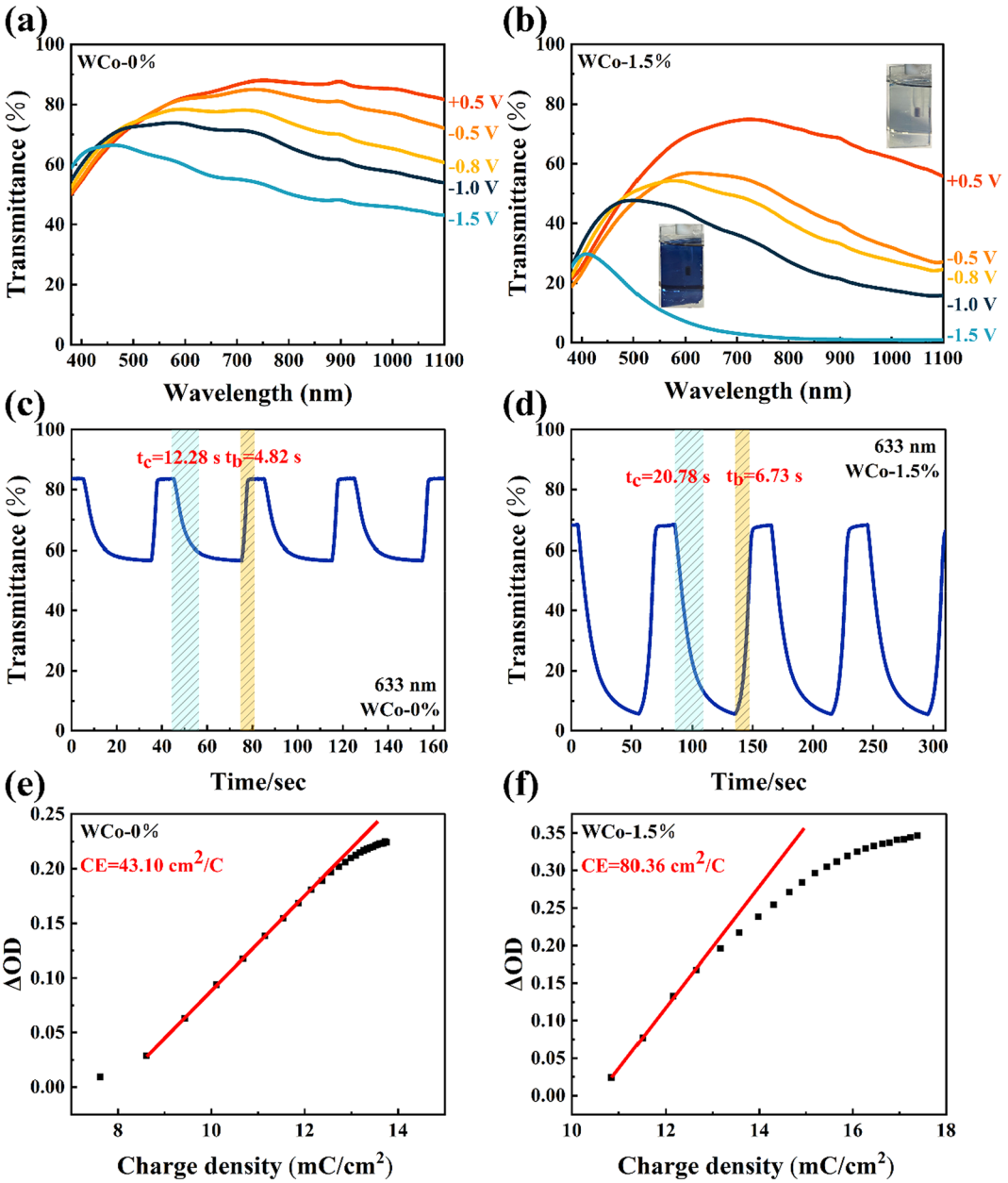

Fig. 8 Transmittance spectra of (a) WO_3 and (b) WCo-1.5% films at different applied potentials (*vs.* Ag/AgCl) for 60 s in the bleached and colored states; the insets are the graphs corresponding to WCo-1.5%; *in situ* response curves of (c) WO_3 and (d) WCo-1.5% films at a wavelength of 633 nm; (e) WO_3 and (f) WCo-1.5% films at 633 nm optical density (ΔOD) *vs.* charge density ($\Delta Q/S$) curves at 633 nm.

Table 1 The optical modulation and switching times of WO_3 films with Co doping at different ratios

	Optical modulation range (%)		Switching time (s)	
Sample	633 nm	899 nm	t_b	t_c
WCo-0%	30.73	39.24	4.82	12.28
WCo-0.5%	40.58	57.25	5.67	12.37
WCo-1.0%	45.04	58.91	5.74	13.92
WCo-1.5%	66.26	72.57	6.73	20.78
WCo-2.0%	28.09	48.42	8.35	36.35

Fig. 10(a) depicts the doping process of Co ions in the hexagonal phase WO_3. The substitution of W ions by Co ions leads to a minor distortion of the lattice structure, which causes the surface of the nanorods to become rough due to nanoscale irregularities, which is verified by TEM analysis. Simultaneously, Co doping results in the formation of additional lattice defects in WO_3, including oxygen vacancies. However, the hexagonal phase of WO_3 is maintained, as confirmed by XPS and XRD analyses. As illustrated in Fig. 10b, the preservation of channels in the hexagonal phase ensures the superior cycling stability of the WO_3 material, which is in

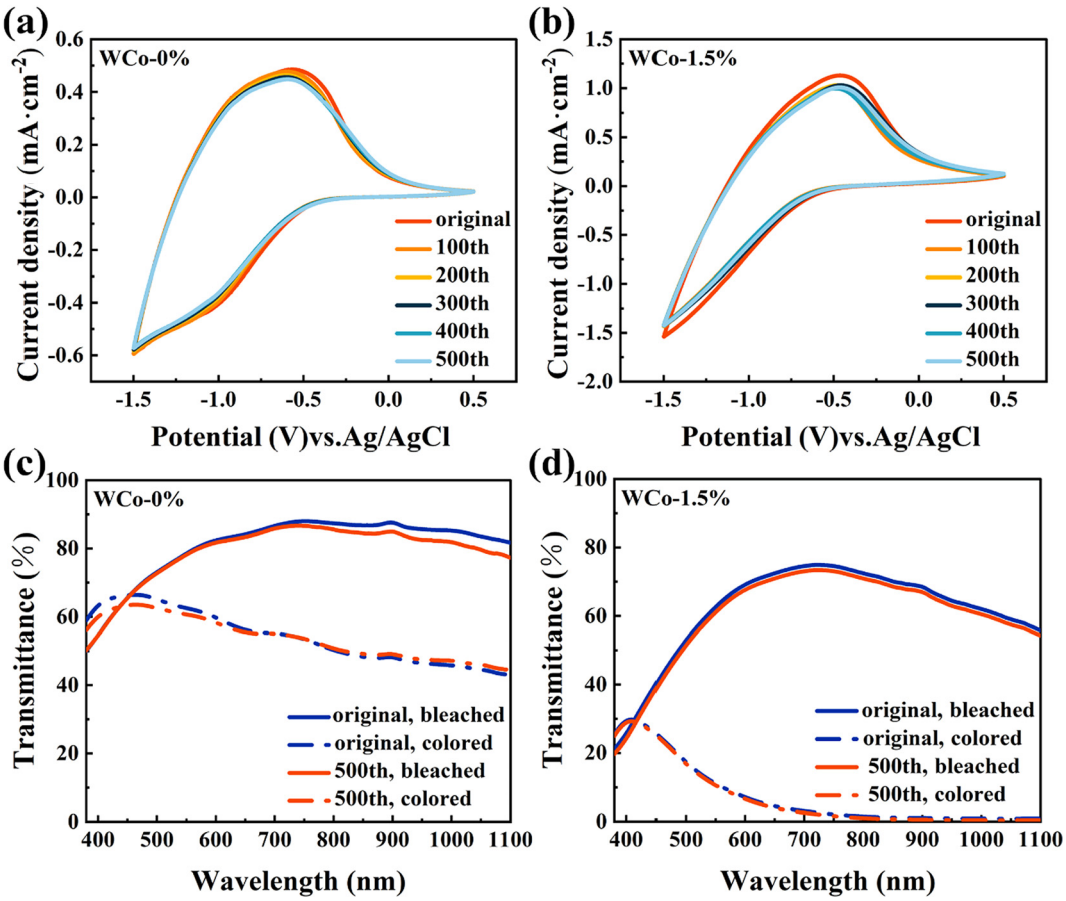

Fig. 9 (a and b) Cyclic voltammetry curves and (c and d) transmittance spectra of WO_3 and WCo-1.5% films in the original state and after 500 cycles.

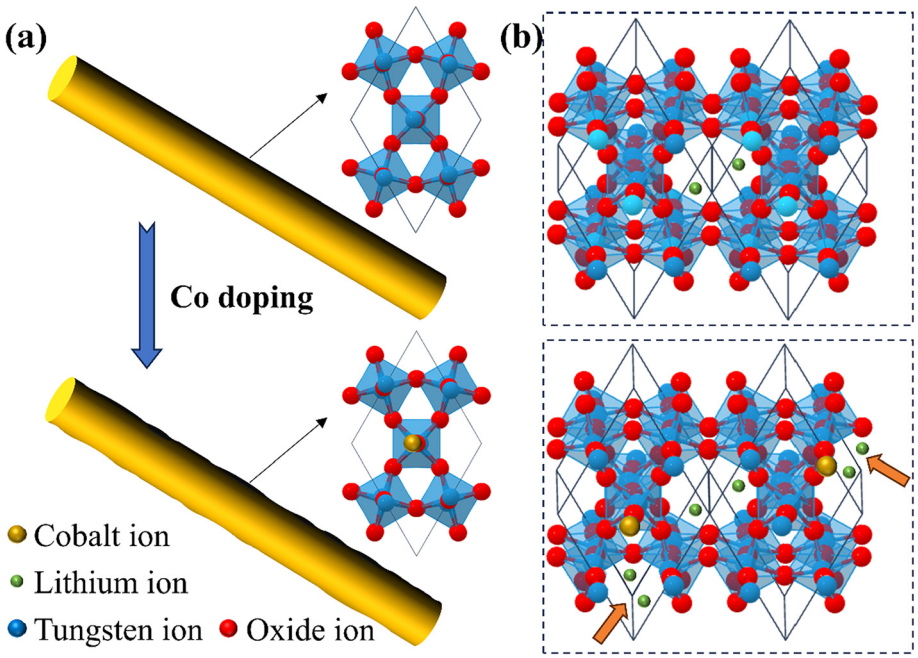

Fig. 10 (a) Co ion doping of hexagonal phase WO_3 and (b) its electrochromic process diagram.

accordance with the test results obtained in Fig. 9. Moreover, the morphological alterations and abundant oxygen vacancies introduced by Co doping facilitate enhanced contact between WO_3 and the electrolyte, increasing the number of reactive sites. The oxygen vacancies generated by Co doping provide additional sites for the insertion and extraction of Li ions (indicated by the arrows), thereby enabling Co-doped WO_3 to exhibit excellent optical modulation and coloring efficiency (Fig. 8).

4 Conclusion

In conclusion, hexagonal phase WO_3 nanorod films with varying concentrations of cobalt ions were successfully prepared using a simple hydrothermal method. The introduction of cobalt ions induces significant changes in the internal micromorphology and chemical state of the WO_3 films, which in turn leads to a substantial alteration in their electrochromic properties. Compared with pure WO_3, it was found that low concentration (1.5%) cobalt-doped WO_3 exhibits excellent electrochromic properties, achieving a high optical modulation (66.27% at 633 nm and 72.57% at 890 nm), a high coloration efficiency (80.36 cm^2 C^{-1} at 633 nm) and remarkable cycling stability (maintained 98.55% after 500 cycles). The enhanced overall performance may be attributed to the large specific surface area, low crystallinity, and nanorod structure that promote lithium-ion diffusion, which is facilitated by cobalt doping. In contrast, a high concentration of cobalt doping results in a significant decrease in the performance of WO_3 films, primarily due to the formation of cobalt oxides on the film surface and substantial lattice distortion caused by excessive doping.

Author contributions

This manuscript is the work of all authors. All the authors agreed on the final version of the manuscript.

Zhaozhu Qu: conceptualization, investigation, formal analysis, and writing – original draft. Ankang Li: conceptualization, investigation, formal analysis, and writing – original draft. Ming Gao: formal analysis. Xiaohui Sun: writing – review & editing. Xuyang Zhang: writing – review & editing, supervision, and funding acquisition. Guohua Wu: writing – review & editing, supervision, and funding acquisition. Xiangwei Wang: supervision, funding acquisition, and project administration.

Data availability

All data supporting this document are included in the paper or its ESI.†

Conflicts of interest

There are no conflicts to declare.

Acknowledgements

This study was supported by the National Natural Science Foundation of China (52103223), the Natural Science Foundation of Heilongjiang Province of China (YQ2023E027), and the Key Laboratory of Functional Molecular Solids, Ministry of Education (No. FMS20230010).

References

1 L. Qin, Y. Liu, M. Long, B. Zou and S. Cao, *Ceram. Int.*, 2024, **50**, 22174–22183.
2 L. Wang, Y. Liu, G. Han and H. Zhao, *Sol. Energy Mater. Sol. Cells*, 2023, **250**, 112053.
3 L. Zhang, G. Xia, X. Li, G. Xu, B. Wang, D. Li, A. Gavrilyuk, J. Zhao and Y. Li, *Synth. Met.*, 2019, **248**, 88–93.
4 Q. Zhao, Z. Pan, B. Liu, C. Bao, X. Liu, J. Sun, S. Xie, Q. Wang, J. Wang and Y. Gao, *Nano Lett.*, 2023, **15**, 87.
5 D.-K. Bui, T. N. Nguyen, A. Ghazlan and T. D. Ngo, *Appl. Energy*, 2021, **300**, 117341.
6 H. Li, C. J. Firby and A. Y. Elezzabi, *Joule*, 2019, **3**, 2268–2278.
7 K. Wang, H. Wu, Y. Meng, Y. Zhang and Z. Wei, *Energy Environ. Sci.*, 2012, **5**, 8384–8389.
8 J. Chen and P. S. Lee, *Adv. Energy Mater.*, 2020, **11**, 2003311.
9 J. Yan, S. Li, B. Lan, Y. Wu and P. S. Lee, *Adv. Funct. Mater.*, 2019, **30**, 1902564.
10 M. H. Elshorbagy and R. Ramadan, *Energies*, 2023, **16**, 2327.
11 T. Rao, Y. Zhou, J. Jiang, P. Yang and W. Liao, *Nano Energy*, 2022, **100**, 107479.
12 L. Wang, Y. Liu, G. Han and H. Zhao, *J. Alloys Compd.*, 2022, **890**, 161833.
13 Y.-C. Her and C.-C. Chang, *CrystEngComm*, 2014, **16**, 5379–5386.
14 K. Tang, Y. Zhang, Y. Shi, J. Cui, X. Shu, Y. Wang, Y. Qin, J. Liu, H. H. Tan and Y. Wu, *Appl. Surf. Sci.*, 2019, **498**, 143796.
15 K. Ghosh, A. Roy, S. Tripathi, S. Ghule, A. K. Singh and N. Ravishankar, *J. Mater. Chem. C*, 2017, **5**, 7307–7316.
16 M. Li, W. Jiang, Y. Lin, C. Huang, P. Hao, W. Wang, L. Yang, Y. Wang and D. Wang, *J. Mater. Chem. C*, 2024, **12**, 5420–5430.
17 R. R. Kharade, S. S. Mali, S. P. Patil, K. R. Patil, M. G. Gang, P. S. Patil, J. H. Kim and P. N. Bhosale, *Electrochim. Acta*, 2013, **102**, 358–368.
18 S. Balaji, Y. Djaoued and A. Albert, *Chem. Mater.*, 2009, **21**, 1381–1389.
19 X. Huo, H. Zhang, W. Shen, X. Miao, M. Zhang and M. Guo, *J. Mater. Chem. A*, 2019, **7**, 16867–16875.
20 S. Adhikari and D. Sarkar, *J. Electrochem. Soc.*, 2014, **162**, H58–H64.
21 C.-H. Lu, M. H. Hon and I.-C. Leu, *J. Electron. Mater.*, 2016, **46**, 2080–2084.
22 J. Wang, E. Khoo, P. S. Lee and J. Ma, *J. Phys. Chem. C*, 2009, **113**, 9655–9658.

23 G. T. Phan, D. V. Pham, R. A. Patil, C.-H. Tsai, C.-C. Lai, W.-C. Yeh, Y. Liou and Y.-R. Ma, *Sol. Energy Mater. Sol. Cells*, 2021, **231**, 111306.
24 F. Azimi Dalenjan, M. M. Bagheri-Mohagheghi and A. Shirpay, *Opt. Quantum Electron.*, 2022, **54**, 711.
25 W. Q. Wang, Z. J. Yao, X. L. Wang, X. H. Xia, C. D. Gu and J. P. Tu, *J. Colloid Interface Sci.*, 2019, **535**, 300–307.
26 D. M. Kabtamu, J.-Y. Chen, Y.-C. Chang and C.-H. Wang, *J. Mater. Chem. A*, 2016, **4**, 11472–11480.
27 M. A. Arvizu, G. A. Niklasson and C. G. Granqvist, *Chem. Mater.*, 2017, **29**, 2246–2253.
28 B. Wang, W. K. Man, H. Y. Yu, Y. Li and F. Zheng, *Materials*, 2018, **11**, 1627.
29 J. Su, X. Feng, J. D. Sloppy, L. Guo and C. A. Grimes, *Nano Lett.*, 2011, **11**, 203–208.
30 G. F. Cai, J. P. Tu, D. Zhou, X. L. Wang and C. D. Gu, *Sol. Energy Mater. Sol. Cells*, 2014, **124**, 103–110.
31 H. Yu, J. Guo, C. Wang, J. Zhang, J. Liu, G. Dong, X. Zhong and X. Diao, *Electrochim. Acta*, 2020, **332**, 135504.
32 K. Shen, K. Sheng, Z. Wang, J. Zheng and C. Xu, *Appl. Surf. Sci.*, 2020, **501**, 144003.
33 D. Ma, G. Shi, H. Wang, Q. Zhang and Y. Li, *J. Mater. Chem. A*, 2013, **1**, 684–691.
34 Z. Jiao, X. W. Sun, J. Wang, L. Ke and H. V. Demir, *J. Phys. D: Appl. Phys.*, 2010, **43**, 285501.
35 F. Zheng, M. Guo and M. Zhang, *CrystEngComm*, 2013, **15**, 277–284.
36 Z. Liu, B. Liu, W. Xie, H. Li, R. Zhou, Q. Li and T. Wang, *Sens. Actuators, B*, 2016, **235**, 614–621.
37 D. Kanchan Kumar, P. Bharathi, J. Archana, M. Navaneethan and S. Harish, *Sens. Actuators, B*, 2024, **421**, 136477.
38 J. Li, Y. Liu, Z. Zhu, G. Zhang, T. Zou, Z. Zou, S. Zhang, D. Zeng and C. Xie, *Sci. Rep.*, 2013, **3**, 2409.
39 H. Ling, J. Lu, S. Phua, H. Liu, L. Liu, Y. Huang, D. Mandler, P. S. Lee and X. Lu, *J. Mater. Chem. A*, 2014, **2**, 2708–2717.
40 K. Tang, Y. Zhang, Y. Shi, J. Cui, X. Shu, Y. Wang, J. Liu, J. Wang, H. H. Tan and Y. Wu, *J. Mater. Chem. C*, 2018, **6**, 12206–12216.
41 M. Saleem, M. F. Al-Kuhaili, S. M. A. Durrani, A. H. Y. Hendi, I. A. Bakhtiari and S. Ali, *Int. J. Hydrogen Energy*, 2015, **40**, 12343–12351.